

# Proposal for semiconductor-free negative differential resistance tunnel diode with ultra-high peak-to-valley current ratio

Ersoy Şaşıoğlu<sup>1\*</sup> and Ingrid Mertig<sup>1,2</sup>

<sup>1</sup>*Institute of Physics, Martin Luther University Halle-Wittenberg, 06120 Halle (Saale), Germany*

<sup>2</sup>*Max Planck Institute of Microstructure Physics, Weinberg 2, 06120 Halle (Saale), Germany*

(Dated: October 26, 2022)

The negative differential resistance (NDR) tunnel diodes are promising alternative devices for beyond-CMOS computing as they offer several potential applications when integrated with transistors. We propose a novel semiconductor-free NDR tunnel diode concept that exhibits ultra-high peak-to-valley current ratio (PVCR) value. Our proposed NDR diode consists of two cold metal electrodes separated by a thin insulating tunnel barrier. The NDR effect stems from the unique electronic band structure of the cold metal electrodes, i.e., the width of the isolated metallic bands around the Fermi level as well as the energy gaps separating higher- and lower-lying bands determine the current-voltage ( $I$ - $V$ ) characteristics and the PVCR value of the tunnel diode. By proper choice of the cold metal electrode materials, either a conventional N-type or  $\Lambda$ -type NDR effect can be obtained. Two-dimensional (2D) nanomaterials offer a unique platform for the realization of proposed NDR tunnel diodes. To demonstrate the proof of concept we employ the nonequilibrium Green function method combined with density functional theory to calculate the  $I$ - $V$  characteristic of the lateral ( $\text{AlI}_2/\text{MgI}_2/\text{AlI}_2$ ) and vertical ( $\text{NbS}_2/\text{h-BN}/\text{NbS}_2$ ) heterojunction tunnel diodes based on 2D cold metals. For the lateral tunnel diode, we obtain a  $\Lambda$ -type NDR effect with an ultra-high PVCR value of  $10^{16}$  at room temperature, while the vertical tunnel diode exhibits a conventional N-type NDR effect with a smaller PVCR value of about  $10^4$ . The proposed concept provides a semiconductor-free solution for NDR devices to achieve desired  $I$ - $V$  characteristics with ultra-high PVCR values for memory and logic applications.

PACS numbers:

## I. INTRODUCTION

Current logic and memory devices are based on the complementary metal oxide semiconductor (CMOS) field-effect transistor technology and more than forty years chip makers have succeeded in scaling of CMOS transistors, which allowed Moore's law to remain on track[1]. However, the 2D scaling of the CMOS technology will reach fundamental limits soon according to the International Roadmap for Devices and Systems[2]. In future technology nodes the performance benefits of CMOS-based devices might no longer meet the circuit performance targets and thus require a hybrid circuit solution. Within the last two decades several beyond-CMOS device concepts ranging from electronic to spintronic, from ferroelectric to resistive switching devices have been proposed and demonstrated [3–7]. Despite many valuable features of these new devices, extensive benchmark calculations have shown that none of them can beat CMOS transistors [8]. Thus, most of the beyond-CMOS devices aim to complement CMOS rather than replace it and they might enable computing paradigms beyond the capabilities of conventional CMOS technology.

The negative differential resistance (NDR) tunnel diodes offer variety of unique functionalities and potential applications when integrated with conventional CMOS

transistors[9]. Among them, NDR-based multi-valued logic gates and static random-access-memory (SRAM) are the most promising applications [10, 11]. The NDR effect allows to design logic and memory architectures with much reduced device count, very high speed, and much lower power consumption. For instance, a tunnel SRAM requires a single transistor and two NDR tunnel diodes instead of six transistors in conventional SRAM architecture, which substantially reduces the device footprint area and power consumption [11, 12]. By employing two NDR diodes connected in series the monostable-bistable transition logic element gate has been demonstrated to perform NAND and NOR operations [13–15]. All other logic gates have also been implemented by combining NDR diodes with CMOS transistors [15]. The binary NDR-based logic has also been extended to the multi-valued logic, which increases the information density per given unit device and decreases the overall system complexity [16–18]. By shifting from binary to the ternary logic the system complexity can be drastically reduced to 63% [19].

There are several devices (two-terminal tunnel diodes) and circuits described in the literature that produce an NDR effect. Of the two-terminal tunnel diodes, the Esaki diode and the resonant tunneling diode received the most attention [20–22]. The Esaki diode is a heavily doped (degenerate) p-n junction diode, in which the electron transport in the contact region is via quantum mechanical tunneling under forward bias and it shows NDR effect, i.e., electrical current decreases with increasing bias voltage. Figure 1 schematically illustrates the current-

---

\*Electronic address: [ersoy.sasioglu@physik.uni-halle.de](mailto:ersoy.sasioglu@physik.uni-halle.de)

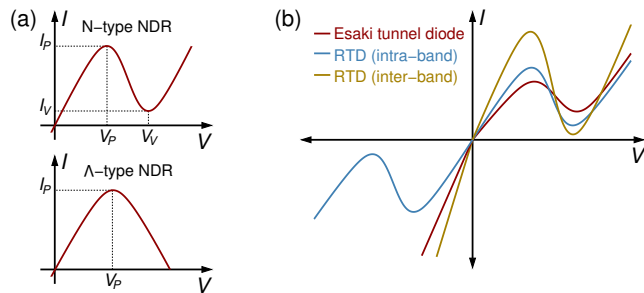


FIG. 1: (Color online) (a) N-type and  $\Lambda$ -type negative differential resistance (NDR). (b) Schematic representation of the current-voltage ( $I$ - $V$ ) characteristics of an Esaki tunnel diode and intra- and inter-band resonant-tunneling diodes.

voltage ( $I$ - $V$ ) characteristics of an Esaki diode and an intra- and inter-band resonant tunneling diodes. However, those two-terminal NDR diodes have two primary features hindering their applications: i) the peak-to-valley current ratio (PVCr) is rather low in tunnel diodes that are compatible with CMOS technology [22–25]. In these diodes the PVCr is usually less than ten, not high enough for memory applications (tunnel SRAM). ii) the III-V semiconductors that produce high PVCr (between 5 and 144) are not compatible with current CMOS technology [26, 27]. The low PVCr values in two-terminal NDR tunnel diodes have been attributed to the band tails tunneling, which originates from the strong doping and doping fluctuations and it has been studied in detail by many authors using different approaches [28–30]. Many research contributions have been reported to improve the PVCr value over 100 based on a CMOS compatible process. Extremely high, by 2-3 orders of magnitude, PVCr values have been obtained in NDR circuits based on combination of a Si-based CMOS and a SiGe heterojunction-bipolar-transistor [31–35]. Despite their high PVCr values, such devices possess complex circuit topology with at least three (four) transistors for a  $\Lambda$ -type (N-type) NDR effect (see Figure 1), which makes them unsuitable for memory applications [36].

Recently, we proposed a new semiconductor-free NDR tunnel diode concept with ultra-high PVCr. A patent application has been filed for the proposed device [37] and preliminary results have been presented in Ref.[38]. Our proposed NDR diode consists of two cold metal electrodes separated by a thin insulating tunnel barrier. In Figure 2 we schematically show the density of states (DOS) of a cold metal and compare with a normal metal and semiconductor. The NDR effect stems from the unique electronic band structure of the cold metal electrodes, i.e., the width of the isolated metallic bands around the Fermi level as well as the energy gaps separating higher and lower lying bands determine the current-voltage ( $I$ - $V$ ) characteristics and the PVCr value of the tunnel diode. By proper choice of the cold metal electrode materials either conventional N-type or  $\Lambda$ -type NDR effect can be obtained. In this paper we provide a detailed description of

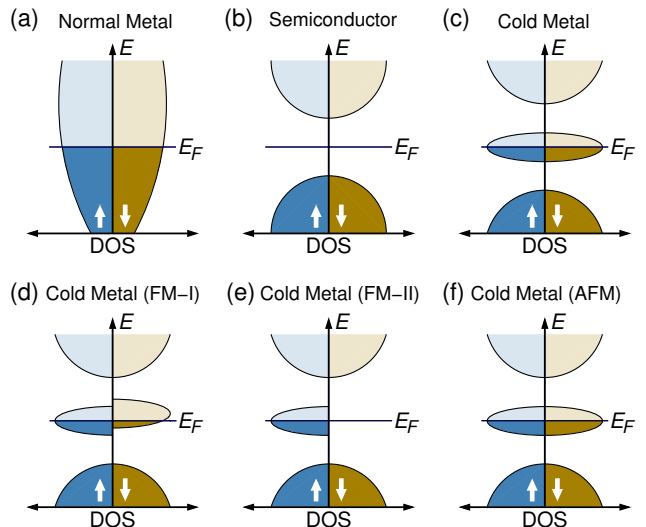


FIG. 2: (Color online) Schematic representation of the density of states (DOS) for (a) a normal metal, (b) a semiconductor, (c) a non-magnetic (or paramagnetic) cold-metal, (d) a ferromagnetic (FM-I) cold-metal, (e) a half-metallic ferromagnetic (FM-II) cold-metal, and (f) an antiferromagnetic (AFM) cold-metal.

the new NDR tunnel diode concept and demonstrate the proof of principle by *ab initio* quantum transport calculations. Furthermore, we address different classes of suitable materials for realizing the new concept. To demonstrate both  $\Lambda$ -type and N-type NDR effects we choose two different kinds of cold metal materials:  $\text{AlI}_2$  and  $\text{NbS}_2$  (see Table I). The former possesses a narrow metallic band around the Fermi level and relatively large energy gaps below and above the Fermi energy, while for the latter material the width of the metallic band and energy gaps are more or less comparable. By employing the nonequilibrium Green function (NEGF) method combined with density functional theory (DFT) we have calculated the  $I$ - $V$  curves of the lateral  $\text{AlI}_2/\text{MgI}_2/\text{AlI}_2$  and vertical  $\text{NbS}_2/\text{h-BN}/\text{NbS}_2$  heterojunction tunnel diodes. We obtain a  $\Lambda$ -type NDR effect for the lateral tunnel diode with an ultra-high PVCr value of  $10^{16}$  at room temperature, while the vertical tunnel diode exhibits conventional N-type NDR effect with a smaller PVCr value of  $10^4$  within the coherent tunneling transport model.

## II. DEVICE CONCEPT

The structure of the proposed cold metal tunnel diode and its  $I$ - $V$  characteristics are shown schematically in Figure 3a. Analogous to the metal-insulator-metal diode, the NDR diode consists of two cold metal electrodes separated by a thin insulating tunnel barrier. Cold metals possess unique electronic band structure (see Figure 3 and Figure 4), i.e., isolated metallic bands around the Fermi energy are separated from the higher-lying and lower-lying states by sizeable energy gaps. The  $I$ - $V$  char-

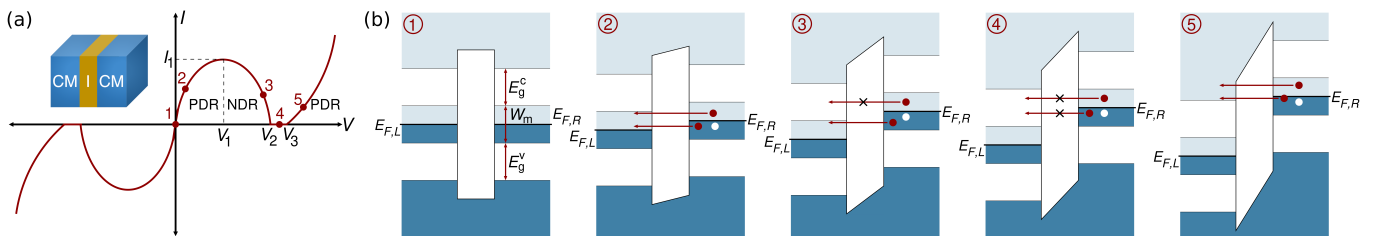


FIG. 3: (Color online) (a) Schematic representation of the cold metal NDR tunnel diode and the corresponding current-voltage ( $I$ - $V$ ) characteristics. (b) A schematic representation of the band diagram and thermal electron-hole excitations for the cold metal NDR tunnel diode for different forward bias voltages.

acteristics of the cold metal tunnel diode can be qualitatively explained on the basis of the schematic energy-band diagram shown in Figure 3b, where the energy-band diagram of the insulating tunnel barrier is represented by a rectangular potential without bias voltage and by a trapezoid when a finite bias is applied. The metallic band width and energy gaps below and above the Fermi level are denoted by  $W_m$ ,  $E_g^V$ , and  $E_g^C$ , respectively. In energy-band diagram (Figure 3b) we assume that  $W_m = E_g^V = E_g^C$ . If we choose the same cold metal materials for the left and right electrodes of the tunnel diode, then no charge transfer takes place between the electrodes.

For a qualitative discussion of the NDR diode characteristics we will use Bardeen's approach for tunneling [39, 40]. For a simple tunnel barrier the tunneling current  $I(V)$  for a bias voltage  $V$  is given by the expression  $I(V) \sim \int_{-\infty}^{+\infty} \rho_{CM}(E + eV) \rho_{CM}(E) |T(V)|^2 f(E) [1 - f(E + eV)] dE$ , where  $\rho_{CM}(E + eV)$  denotes the density of states of the cold metal electrode and  $f(E)$  being the Fermi distribution function.  $T(V)$  is the transmission probability being proportional to  $e^{-d\sqrt{\phi - V}}$ , where  $d$  is the thickness of the tunnel barrier and  $\phi$  being the barrier height. As shown in Figure 3b when a positive bias voltage is applied to the left cold metal electrode (second panel in Figure 3b), electrons from the occupied valence band of the right cold metal electrode tunnel through the insulating barrier into the unoccupied states of the left electrode. With increasing bias voltage  $V$  the current  $I$  increases up to a peak value  $I_1$  then it starts to decrease (panel 3) and finally for a specific value of bias voltage  $V_2$  the current becomes zero. This stems from the fact that the conduction band of the left cold metal electrode has an energy gap  $E_g^C$  and thus within the applied potential window there are no available states for the electrons to tunnel into (see panel 4), resulting in a zero current. At zero temperature this current is exactly zero, while at finite temperature very few thermally excited high energy electrons that are at the tail of the Fermi-Dirac distribution of the right cold metal electrode can tunnel into the left electrode giving rise to an extremely small current and thus the PVCr takes a finite value instead of an infinite value at room temperature. The current remains zero between the bias potential  $V_2$  and  $V_3$  and after  $V_3$  the current starts to increase again. The region between the

bias potential  $V_1$  and  $V_2$  is called the NDR region. The current in the first positive differential resistance (PDR) region and in NDR region (see Figure 3a) stems from the intra-band tunneling, while in the second PDR region it is due to the inter-band tunneling (panel 5 in Figure 3b). Note that the applied bias voltage drops across the insulating tunnel barrier.

The  $I$ - $V$  characteristics of a cold metal tunnel diode having the same left and right electrodes is mainly determined by three parameters  $W_m$ ,  $E_g^V$ , and  $E_g^C$ . For N-type NDR effect one of the the following three conditions should be satisfied: i)  $W_m \sim E_g^V \sim E_g^C$ , ii)  $W_m \sim E_g^C < E_g^V$ , iii)  $W_m \sim E_g^V < E_g^C$ . In this case  $V_2 \simeq V_3$  in  $I$ - $V$  characteristics shown in Figure 3a. When none of these three conditions are satisfied the NDR effect can still be observed but with a substantially reduced PVCr value. For a  $\Lambda$ -type NDR effect the metallic band width should be much smaller than the both energy gaps, i.e.,  $W_m \ll E_g^V \sim E_g^C$  and this leads to  $V_2 \ll V_3$  in  $I$ - $V$  characteristics. For both types of NDR effects the bias voltages  $V_1$  and  $V_2$  corresponding to the peak and valley currents are approximately determined by  $W_m/2$  and  $W_m$ , respectively.

Up to now we focus only on the forward bias and discuss the NDR effect. In the same way, for a reverse bias one can observe the same NDR effect, i.e., the  $I$ - $V$  characteristics of the cold metal tunnel diode turns out to be anti-symmetric if the left and right electrodes are made of the same materials. This is similar to the intra-band resonant tunneling diode but different than the Esaki diode and inter-band resonant tunneling diode shown in Figure 1b. As the  $I$ - $V$  characteristics of the cold metal tunnel diode mainly depends on the three electronic structure parameters  $W_m$ ,  $E_g^V$ , and  $E_g^C$ , by proper choice of the left and right electrode materials one can achieve desired  $I$ - $V$  characteristics. For instance, the NDR region ( $V_1$ - $V_2$  interval) can be tuned by tuning these parameters. Moreover, multi-peak NDR effect can be achieved in cold metal tunnel diodes connected in series.

Cold metallic behaviour is rather rare among the three-dimensional (3D) bulk materials. Known examples are alkali-doped fullerenes [41], high temperature paramagnetic phase of  $V_2O_3$  [42], and recently several flat-band materials such as  $CoAl_2O_4$ ,  $Rb_2NbCl_6$ ,  $Sr_3PbNiO_6$ , etc have been predicted to show cold metallic behaviour [43].

On the other hand, two-dimensional (2D) transition-metal dichalcogenides ( $\text{NbX}_2$ ,  $\text{TaX}_2$ ,  $\text{X}=\text{S, Se, Te}$ ) and transition-metal dihalides ( $\text{ScI}_2$ ,  $\text{YI}_2$ , etc) as well as several other 2D materials like  $\text{AlI}_2$ ,  $\text{GaI}_2$ ,  $\text{InI}_2$ ,  $\text{Ag}_2\text{F}_4$ ,  $\text{DySBr}$ ,  $\text{DySI}$ ,  $\text{NdOBr}$ ,  $\text{SmOBr}$ , etc exhibit cold-metallic behaviour [44–46] and offer a unique platform for the realization of the proposed NDR tunnel diodes. Moreover, in contrast to 3D materials, 2D materials are much better suited for tunneling devices as they form high-quality heterointerfaces due to the absence of dangling bonds. Recently conventional N-type NDR effect has been observed in a variety of devices based on 1D[47, 48] and 2D materials, such as graphene/h-BN/graphene resonant tunnel diodes,[49] black phosphorus tunnel diodes [50, 51], as well as transition-metal dichalcogenide tunnel diodes [52–54]. However, in all these 2D material based NDR tunnel devices the PVCR values were found to be less than 10 and thus they do not exhibit their theoretical advantages. As will be shown in the following section the tunnel diodes based on 2D cold metals overcome the limitations of conventional semiconductor tunnel devices by providing ultra-high PVCR values as well as both types of NDR effects, i.e., conventional N-type NDR and  $\Lambda$ -type NDR effect. The latter can be achieved only in multi-terminal NDR circuits.

### III. COMPUTATIONAL METHODS

Ground state electronic structure calculations are carried out using DFT implemented in the QuantumATK S-2021.06 package[55]. As basis-set we use linear combinations of atomic orbitals (LCAO) together with norm-conserving PseudoDojo pseudopotentials[56] with the Perdew-Burke-Ernzerhof (PBE) parametrization of the exchange-correlation functional[57]. We use DFT-D2 van der Waals corrections for the vertical tunnel diode. A dense  $24 \times 24 \times 1$   $\mathbf{k}$ -point grid and density mesh cutoff of 120 Hartree have been used. To prevent interactions between the periodically repeated images, 20 Å of vacuum were added and Dirichlet and Neumann boundary conditions are employed to the upper and lower surface, respectively. The total energy and forces have been converged at least to  $10^{-4}$  eV and 0.01 eV/Å, respectively.

The transport calculations were performed using DFT combined with the NEGF method. We use a  $24 \times 1 \times 172$  ( $8 \times 1 \times 172$ )  $\mathbf{k}$ -point grid in self-consistent DFT-NEGF calculations of lateral (vertical) tunnel diodes. The  $I$ - $V$  characteristics were calculated within a Landauer approach [58], where  $I(V) = \frac{2e}{h} \int T(E, V) [f_L(E, V) - f_R(E, V)] dE$ . Here  $V$  denotes the bias voltage,  $T(E, V)$  is the transmission coefficient and  $f_L(E, V)$  and  $f_R(E, V)$  are the Fermi-Dirac distributions of the left and right electrodes, respectively. The transmission coefficient  $T(E, V)$  for lateral (vertical) tunnel diode is calculated using a  $300 \times 1$  ( $100 \times 1$ )  $\mathbf{k}$ -point grid.

### IV. RESULTS AND DISCUSSION

The cold metal tunnel diode concept introduced in the preceding section can be realized either by using 3D materials or 2D van der Waals materials. In the following, due to their structural simplicity and high-quality heterointerfaces because of the absence of dangling bonds in vertical devices, we will focus on the 2D materials by considering a lateral and a vertical tunnel diode as shown in Table I and demonstrate the proof of principle by *ab-initio* quantum transport calculations. As pointed out above, depending on the electronic band structure parameters ( $W_m$ ,  $E_g^V$ , and  $E_g^C$ ) of the cold metal electrode materials, a tunnel diode showing either conventional N-type or  $\Lambda$ -type NDR effect can be realized. For this purpose, as electrode materials we choose  $\text{AlI}_2$  (1T phase) and  $\text{NbS}_2$  (1H phase) and DFT-PBE electronic band structure of both materials are shown in Figure 4a. As seen, both materials have a single metallic band of similar width ( $W_m$ ) crossing the Fermi level and an energy gap above the Fermi level ( $E_g^C$ ) of similar size. While the energy gap  $E_g^V$  of  $\text{AlI}_2$  below the Fermi energy is much larger than the corresponding energy gap of  $\text{NbS}_2$  (see Table I). Note that our ground-state calculations for both materials are in good agreement with previously published data[44]. As for the case of semiconductors and insulators, the DFT-PBE method underestimates the energy gaps ( $E_g^V$ , and  $E_g^C$ ) of the cold metals under consideration. The accurate  $E_g^V$  and  $E_g^C$  values are of particular importance in tunnel diodes made of transition-metal dichalcogenides as they possess  $E_g^V$  values, which are smaller than the  $W_m$  in DFT-PBE method, which might result in smaller PVCR values. Taking electronic correlations into account either within the HSE06 hybrid functional or  $GW$  method results in larger  $E_g^V$  and  $E_g^C$  values [44, 59, 60]. For computational purposes, in transport calculations we adopt the PBE-1/2 method, which gives rather accurate band gaps in semiconductors and insulator. For instance, PBE gives 4.69 eV for the band gap of h-BN, an insulator used as a tunnel barrier in vertical heterojunction diode, while the PBE-1/2 method more or less reproduces the experimental band gap of 6.1 eV (see Table I). Figure 4b shows the  $W_m$ ,  $E_g^V$ , and  $E_g^C$  values calculated with the PBE and PBE-1/2 methods for one monolayer  $\text{NbX}_2$  and  $\text{TaX}_2$  ( $\text{X}=\text{S, Se, Te}$ ) compounds. As seen in all compounds the  $W_m$  values do not change at all in PBE-1/2 method and also the change of  $E_g^C$  values are negligible. However, PBE-1/2 method gives considerably larger  $E_g^V$  values, which are comparable to the ones obtained by the HSE06 method [44] but larger than the  $GW$  values reported in the literature [59, 60]. Note that the  $GW$  calculations for the electronic band structure of  $\text{NbS}_2$  is in good agreement with the angle-resolved photoemission spectroscopy measurements.[59, 61]

In Figure 5a and 5b, we show the atomic structure of the lateral  $\text{AlI}_2/\text{MgI}_2/\text{AlI}_2$  and vertical  $\text{NbS}_2/\text{h}$ -

TABLE I: Material composition of the tunnel diode, type of NDR effect, crystal structure, lattice constants  $a$ , PBE (PBE-1/2) band gap  $E_g$  of the insulating tunnel barrier, PBE (PBE-1/2) metallic band width  $W_m$ , and energy gaps  $E_g^V$  and  $E_g^C$  below and above the Fermi level for the cold metallic electrode materials. Lattice parameters are taken from Ref. [44].

Tunnel Diode	NDR	Compound	$a(\text{\AA})$	$E_g(\text{eV})$	$W_m(\text{eV})$	$E_g^V(\text{eV})$	$E_g^C(\text{eV})$
All <sub>2</sub> /MgI <sub>2</sub> /All <sub>2</sub>	$\Lambda$ -type	1T-All <sub>2</sub>	4.14		1.20 (0.95)	1.65 (2.96)	1.55 (2.29)
		1T-MgI <sub>2</sub>	4.21	3.66 (5.45)			
NbS <sub>2</sub> /BN/NbS <sub>2</sub>	N-type	1H-NbS <sub>2</sub>	3.34		1.25 (1.20)	0.44 (1.21)	1.36 (1.38)
		h-BN	2.51	4.69 (6.17)			

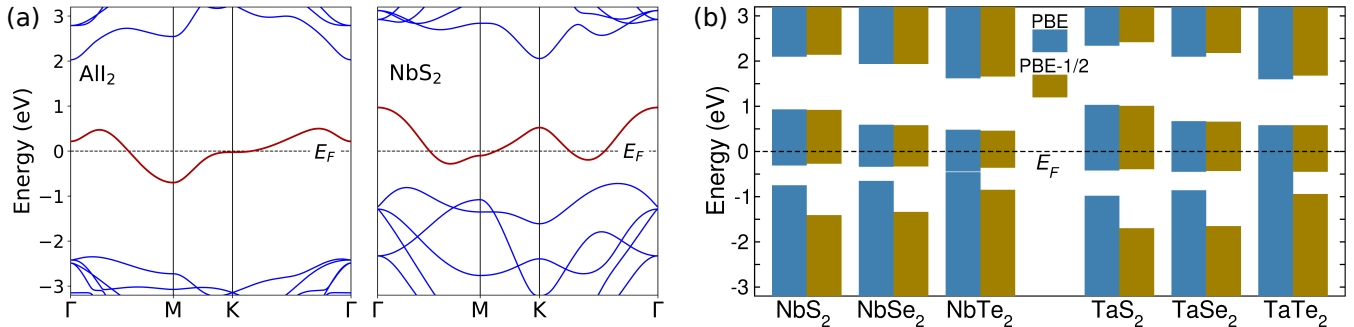


FIG. 4: (Color online) (a) Calculated PBE band structure of the monolayer 1T All<sub>2</sub> and 1H NbS<sub>2</sub> along the high symmetry lines in 2D Brillouin zone. The dashed black lines denote the Fermi level, which is set to zero. (b) PBE and PBE-1/2 method comparison of the metallic band widths ( $W_m$ ), and energy gaps below ( $E_g^V$ ) and above ( $E_g^C$ ) the Fermi level for NbX<sub>2</sub> and TaX<sub>2</sub> (X=S, Se, Te) compounds.

BN/NbS<sub>2</sub> heterojunction tunnel diodes, respectively. The lateral tunnel diode is formed by joining one monolayer of All<sub>2</sub> (left electrode), a one monolayer tunnel barrier MgI<sub>2</sub>, and one monolayer of All<sub>2</sub> (right electrode). Due to the very similar lattice parameters of electrode and tunnel barrier materials (see Table I) as well as their similar compositions, they form a perfect interface. We assume periodicity of the device in the  $x$ -direction. The  $z$ -direction is chosen as the transport direction. We consider both armchair and zigzag orientations and the thickness of tunnel barrier is 7.3  $\text{\AA}$  for the former case and 8.4  $\text{\AA}$  for the latter case. The total length of the scattering region is about 64  $\text{\AA}$  for both orientations. On the other hand, for the vertical tunnel diode the lattice mismatch between NbS<sub>2</sub> and tunnel barrier h-BN is relatively large and thus in device modelling we construct an orthorhombic commensurate supercell of  $3 \times 3$  for NbS<sub>2</sub> and  $4 \times 4$  for h-BN and consider only armchair orientation as shown in Figure 5b with an overlap region of about 24  $\text{\AA}$  and the scattering region is about 70  $\text{\AA}$ .

Next, we discuss the transport properties of the cold metal heterojunction tunnel diodes. In the preceding section we qualitatively discussed the operation principle and  $I$ - $V$  characteristics of a cold metal tunnel diode on the basis of a schematic energy-band diagram of the electrodes and a simple tunnel barrier model. However, in real materials quantum tunneling is a very sophisticated process as it depends on the symmetry of Bloch states in the electrodes, their matching at the interface, and their decay rate, which is determined by thickness and barrier height as well as the complex energy bands of the tunnel

barrier. Thus, fully *ab-initio* atomic scale transport calculations are needed to reveal the  $I$ - $V$  characteristics of the proposed cold metal tunnel diodes. Calculated  $I$ - $V$  curves are presented in Figure 5c and 5d for the lateral and the vertical tunnel diode, respectively. In both tunnel diodes left and right cold metal electrodes are the same and thus we obtain anti-symmetric  $I$ - $V$  curves. In both cases with an applied bias voltage  $V$  the current  $I$  exponentially increases and reaches the peak value  $I_p$  at about 0.15 V and thus the first PDR region in both tunnel diodes is limited to a small bias voltage window of 0.15 V in contrast to rough estimation of 0.48 V and 0.6 V based on the energy-band diagram in preceding section. However, in both tunnel diodes the valley current  $I_v$  is determined by  $W_m$  of electrode materials, i.e., 0.95 eV for All<sub>2</sub> and 1.2 eV for NbS<sub>2</sub> (see Table I), which gives rise to an extended NDR region. At room temperature the valley current in lateral tunnel diode is almost zero, which leads to an ultra-high PVCR value of  $10^{16}$ , while for the vertical tunnel diode the PVCR value is about  $10^4$ , which is still much larger than the conventional semiconductor NDR tunnel diodes. The vertical tunnel diode exhibits N-type NDR effect since the electrode material NbS<sub>2</sub> possesses  $W_m \sim E_g^V \sim E_g^C$  within the PBE-1/2 method and thus the second PDR region starts at about 1.2 V and current increases exponentially as in the first PDR region. On the other hand, as will be discussed in detail in the following for the lateral tunnel diode the  $W_m$  is much smaller than the  $E_g^V$  and  $E_g^C$  (see Figure 6a) and thus the second PDR region starts at bias voltages larger than 2.3 V. Therefore, the NDR effect in the lateral tun-

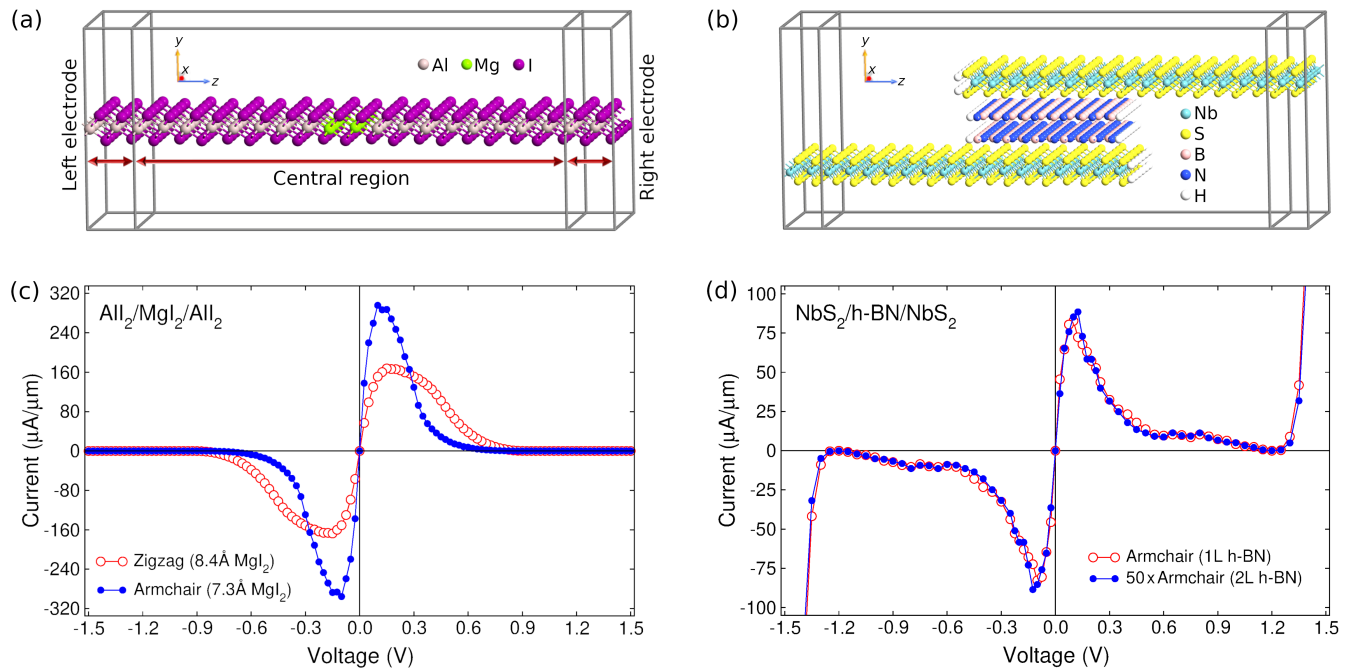


FIG. 5: (Color online) (a) The atomic structure of the lateral AlI<sub>2</sub>/MgI<sub>2</sub>/AlI<sub>2</sub> cold metal tunnel diode. The system is periodic along the x-direction orthogonal to the z-axis, which is the transport direction. (b) The same as (a) for the vertical NbS<sub>2</sub>/h-BN/NbS<sub>2</sub> cold metal tunnel diode. (c) The current-voltage characteristics for the lateral AlI<sub>2</sub>/MgI<sub>2</sub>/AlI<sub>2</sub> tunnel diode in both armchair and zigzag orientations. (d) The same as (c) for the vertical NbS<sub>2</sub>/h-BN/NbS<sub>2</sub> cold metal tunnel diode in armchair orientation.

nel diode can be regarded as a  $\Lambda$ -type NDR.

As expected for both tunnel diodes the current decays exponentially with increasing the tunnel barrier thickness as seen in Figure 5. For instance, the lateral AlI<sub>2</sub>/MgI<sub>2</sub>/AlI<sub>2</sub> tunnel diode having zigzag orientation poses slightly thicker tunnel barrier of about 8.4 Å, which leads to 40% less peak current density compared to the tunnel diode with armchair orientation. The situation is very similar in the case of vertical tunnel diode NbS<sub>2</sub>/h-BN/NbS<sub>2</sub>, in which the current decreases by a factor of 50 from 1 to 2 monolayers of h-BN tunnel barrier. However, the current densities between the lateral and vertical tunnel diodes are very different. For a similar tunnel barrier thicknesses and the same armchair orientations the lateral tunnel diode has almost four times larger peak current density of about 290 μA/μm.

The NDR effect can be explained on the basis of the device density of states (DDOS) (or local DOS). For simplicity we focus only on the lateral tunnel diode and consider the armchair orientation. The calculated DDOS using the PBE-1/2 method for two different bias voltages are presented in Figure 6a. Note that in DDOS the energy resolved number of states are color coded and it can be regarded as the energy-band diagram of the tunnel diode (see Figure 3). As seen from the DDOS and also from the Table I the band width  $W_m$  of the AlI<sub>2</sub> electrode does not change much but  $E_g^V$  and  $E_g^C$  values increases by 1.3 eV and 0.8 eV, respectively within the PBE-1/2 method. The tunnel barrier MgI<sub>2</sub> has a band gap of

about 5.45 eV, which is clearly seen in DDOS. Moreover, the voltage drop across the tunnel barrier is also seen, especially around -3 eV, as a linear change of DDOS (the valence band maximum of MgI<sub>2</sub>) from the right to the left electrode. To get further insight into the drop of bias voltage across the tunnel barrier in Figure 6b we present the electrostatic difference potential  $\Delta V_E$  along the transport direction of the tunnel diode for two different bias voltages. As seen the  $\Delta V_E$  is flat towards the electrodes and it drops linearly across the insulating tunnel barrier revealing that the bias voltage drop takes place at the tunnel barrier. The potential values are given in Volt and the left-to-right potential drop is 0.4 V and 1.2 V, which are exactly the applied bias voltages. Returning back to the discussion of  $I$ - $V$  characteristics, under an applied bias voltage  $V$  the current stems from the intra-band tunneling, i.e., electrons in the occupied states (see Figure 4a) in the right cold metal electrode can tunnel into the unoccupied states of the left cold metal electrode (see also panel 2 in Figure 3b). This tunneling is very efficient at low bias voltages and thus the peak current turns out to be around 0.15 V and bias voltages higher than the  $W_m$  of AlI<sub>2</sub> the intra-band tunneling completely ceases since occupied and unoccupied energy levels are no longer aligned (see panel 4 in Figure 3b). This can also be seen from the transmission spectrum presented in Figure 6c, in which transmission is finite for a bias voltage of 0.4 V, whereas it is exactly zero for 1.2 V, which is larger than the  $W_m$  (0.95 eV) of AlI<sub>2</sub>. It is worth to note that in  $I$ - $V$

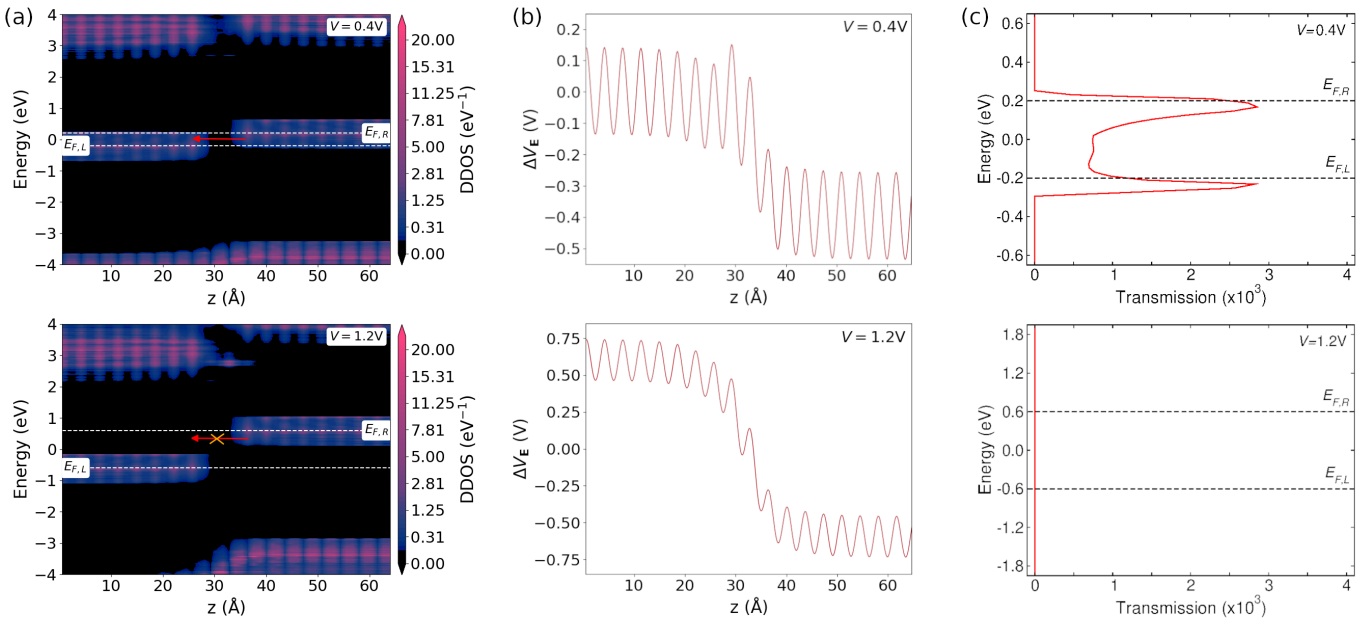


FIG. 6: (Color online) (a) Device density of states (DDOS) for the lateral  $\text{AlI}_2/\text{MgI}_2/\text{AlI}_2$  cold metal tunnel diode for an applied bias voltage of  $V = 0.4\text{ V}$  (upper panel) and  $V = 1.2\text{ V}$  (lower panel) calculated with PBE-1/2 method. The dashed lines display the Fermi level of the left and right electrodes (the corresponding atomic structure is presented in Figure 5a). (b) and (c) calculated electrostatic difference potential and transmission spectrum, respectively.

characteristics of the cold metal tunnel diodes the first PDR and NDR regions stem from the intra-band tunneling, while the second PDR region is due to inter band tunneling. (see panels 2, 3, and 5 in Figure 3b) Note also that finite PVCr values, especially in  $\Lambda$ -type NDR effect originates from the thermal excitations, i.e., very few high energy electrons at the tail of the Fermi-Dirac distribution function could contribute to the valley current.

The  $I$ - $V$  characteristics and the ultra-high PVCr values of the tunnel diodes discussed above are based on the coherent tunneling transport i.e., no dissipation mechanism like inelastic electron-electron scattering or electron-phonon scattering is taken into account in calculations of the  $I$ - $V$  curves. The latter is more efficient in 2D semiconductors than 3D ones [62], giving rise to lower room-temperature mobility and as a result low on currents in field-effect transistors based on 2D semiconducting nanomaterials [63]. The electron-phonon scattering as a dissipation mechanism has been implemented in the QuantumATK package, however due to enormous computational cost of such calculations, it has been only employed to very simple model systems like  $\text{H}_2$  molecule placed between 1D Au chains.[55] Thus, for the present tunnel diodes the inclusion of the electron-phonon scattering in transport calculations is not feasible at all from the computational point of view. Therefore, the peak current  $I_1$  (see Figure 3 and Figure 5) in the  $I$ - $V$  characteristics as well as the PVCr value of the tunnel diodes can be regarded as the upper limit within the coherent tunneling transport approach employed in the present work. Inclusion of the inelastic scattering processes like

electron-phonon interaction is expected to renormalize the  $I$ - $V$  characteristics, i.e., it would decrease (increase) the peak (valley) current and consequently it would reduce the PVCr value. In addition to dissipative processes, defects and interaction with the environment, i.e., the surrounding dielectric materials would also influence the  $I$ - $V$  characteristics of the devices. However, the overall  $I$ - $V$  curves of the tunnel diodes are not expected to change substantially, i.e., one can obtain either a conventional N-type or  $\Lambda$ -type NDR effect by proper choice of the cold metal electrode materials.

Finally we would like to comment on the transport properties of the cold metal  $\text{MX}_2$  ( $\text{M}=\text{Nb, Ta}$ ;  $\text{X}=\text{Se, S}$ ) heterojunctions studied in Ref. [64] and dwell on the other applications of the cold metals in nanoelectronics. The authors of the Ref. [64] claim to get a promising PVCr value of 51 and extremely high peak current density ( $5.1 \times 10^4 \mu\text{A}/\mu\text{m}$ ) for an edge contact  $\text{NbSe}_2/\text{NbS}_2$  heterojunction device. However, we have shown in Supporting Information [65] that the NDR effect obtained in this paper does not stem from a physical mechanism but from the numerical treatment of the current in the QuantumATK package. Cold metals are not only promising materials for NDR tunnel diodes as discussed in this work but also they have been proposed to achieve sub-60 mV/dec subthreshold swing (SS) in a CMOS transistor when used as the source electrode. The unique electronic band structure of the cold metal source electrode in a CMOS transistor filters the transmission of high-energy electrons in the subthreshold region leading to sub-60 mV/dec SS value and also reduces the leakage current in

the off state [66–70]. Besides applications of cold metals in CMOS transistors, in metal-semiconductor Schottky barrier diodes the use of a cold metal electrode instead of normal metal one breaks the thermionic limit of an ideality factor ( $\eta$ ) of 1 at room temperature, which paves the way for the development of low-power electronic circuits [71].

## V. CONCLUSIONS

In conclusion, we proposed a novel semiconductor-free NDR tunnel diode concept that exhibits ultra-high PVCRCR value. The proposed NDR diode consists of two cold metal electrodes separated by a thin insulating tunnel barrier. The operation principle and the NDR effect rely on the unique electronic band structure of the cold metal electrodes, i.e., the width of the isolated metallic bands around the Fermi level as well as the energy gaps separating higher and lower lying bands determine the  $I$ - $V$  characteristics and the PVCRCR value of the tunnel diode. We showed that by proper choice of the cold metal electrode materials either conventional N-type or  $\Lambda$ -type NDR effect can be obtained. In both types of NDR effect the first PDR region and the NDR region are determined by the intra-band quantum tunneling, while inter-band quantum tunneling is responsible for the second PDR region in the  $I$ - $V$  curves of the N-type NDR effect. 2D transition-metal dichalcogenides ( $\text{NbX}_2$ ,  $\text{TaX}_2$ ;  $\text{X}=\text{S}$ ,  $\text{Se}$ ,  $\text{Te}$ ), transition-metal dihalides ( $\text{ScI}_2$ ,  $\text{YI}_2$ , etc),

as well as several other 2D nanomaterials possess cold metallic electronic band structure and offer a unique platform for the realization of the proposed NDR tunnel diodes. We demonstrated the proof of concept by employing the DFT+NEGF method and calculated the  $I$ - $V$  characteristic of the lateral  $\text{AlI}_2/\text{MgI}_2/\text{AlI}_2$  and vertical  $\text{NbS}_2/\text{h-BN}/\text{NbS}_2$  heterojunction tunnel diodes. For the lateral tunnel diode we obtain a  $\Lambda$ -type NDR effect with an ultra-high PVCRCR value of  $10^{16}$  at room temperature, while the vertical tunnel diode exhibits conventional N-type NDR effect with a smaller PVCRCR value of about  $10^4$ . The obtained ultra-high PVCRCR values in tunnel diodes should be regarded as the upper limit as we neglect the dissipative processes like electron-phonon scattering as well as interaction with environment i.e., the surrounding dielectric materials and defects in DFT+NEGF calculations. We anticipate that a plethora of 2D nanomaterials can serve as cold metal electrodes in proposed tunnel diodes to achieve the desired  $I$ - $V$  characteristics and ultra-high PVCRCR values in a semiconductor-free solution for NDR devices for high-speed, low-power memory and logic applications.

## Acknowledgments

E.Ş and I.M. acknowledge support from *Sonderforschungsbereich TRR 227* of Deutsche Forschungsgemeinschaft (DFG) and funding provided by the European Union (EFRE), Grant No: ZS/2016/06/79307.

- 
- [1] G. E. Moore, *Electronics* **38**, 114 (1965).
  - [2] *International Roadmap for Devices and Systems (IRDS)* (2021), available at <https://irds.ieee.org>, URL <https://irds.ieee.org/editions/2021>.
  - [3] A. Chen, J. Hutchby, V. Zhirnov, and G. Bourianoff, *Emerging Nanoelectronic Devices* (John Wiley & Sons, 2014).
  - [4] A. M. Ionescu and H. Riel, *Nature* **479**, 329 (2011).
  - [5] D. E. Nikonov, G. I. Bourianoff, and T. Ghani, *IEEE Electron Device Lett.* **32**, 1128 (2011).
  - [6] I. Amlani, A. O. Orlov, G. Toth, G. H. Bernstein, C. S. Lent, and G. L. Snider, *Science* **284**, 289 (1999).
  - [7] D. A. Allwood, G. Xiong, C. C. Faulkner, D. Atkinson, D. Petit, and R. P. Cowburn, *Science* **309**, 1688 (2005).
  - [8] C. Pan and A. Naeemi, *IEEE J. Explor. Solid-State Comput. Devices Circuits* **3**, 101 (2017).
  - [9] P. R. Berger and A. Ramesh, in *Comprehensive Semiconductor Science and Technology* (Elsevier Inc., 2011), pp. 176–241.
  - [10] S. B. Jo, J. Kang, and J. H. Cho, *Advanced Science* **8**, 2004216 (2021).
  - [11] J. Van Der Wagt, *Proceedings of the IEEE* **87**, 571 (1999).
  - [12] K. Karda, J. Brockman, S. Sutar, A. Seabaugh, and J. Nahas, in *2009 IEEE International Conference on IC Design and Technology* (IEEE, 2009), pp. 233–236.
  - [13] K. J. Chen, K. Maezawa, and M. Yamamoto, *IEEE Electron Device Lett.* **17**, 127 (1996).
  - [14] K. Maezawa, H. Matsuzaki, M. Yamamoto, and T. Otsuji, *IEEE Electron Device Lett.* **19**, 80 (1998).
  - [15] W. Williamson, S. B. Enquist, D. H. Chow, H. L. Dunlap, S. Subramaniam, P. Lei, G. H. Bernstein, and B. K. Gilbert, *IEEE J. Solid-State Circuits* **32**, 222 (1997).
  - [16] L. J. Micheel and M. J. Paulus, in *Proceedings of the Twentieth International Symposium on Multiple-Valued Logic* (IEEE Computer Society, 1990), pp. 189–190.
  - [17] H. Lin, in *Proceedings of 24th International Symposium on Multiple-Valued Logic (ISMVL'94)* (IEEE, 1994), pp. 188–195.
  - [18] N. Jin, S.-Y. Chung, R. M. Heyns, P. R. Berger, R. Yu, P. E. Thompson, and S. L. Rommel, *IEEE Electron Device Lett.* **25**, 646 (2004).
  - [19] S. L. Hurst, *IEEE Trans. Comput.* **33**, 1160 (1984).
  - [20] L. Esaki, *Phys. Rev.* **109**, 603 (1958).
  - [21] L. Esaki and R. Tsu, *IBM J. Res. Dev.* **14**, 61 (1970).
  - [22] A. Ramesh, P. R. Berger, and R. Loo, *Appl. Phys. Lett.* **100**, 092104 (2012).
  - [23] W. Y. Fung, L. Chen, and W. Lu, *Appl. Phys. Lett.* **99**, 092108 (2011).
  - [24] R. Duschl, O. G. Schmidt, G. Reitemann, E. Kasper, and K. Eberl, *Electron. Lett.* **35**, 1111 (1999).
  - [25] H. Schmid, C. Bessire, M. T. Björk, A. Schenk, and H. Riel, *Nano Lett.* **12**, 699 (2012).



- [26] D. H. Chow, J. N. Schulman, E. Özbay, and D. M. Bloom, *Appl. Phys. Lett.* **61**, 1685 (1992).
- [27] H. Tsai, Y. Su, H. Lin, R. Wang, and T. Lee, *IEEE Electron Device Lett.* **15**, 357 (1994).
- [28] S. Sant and A. Schenk, *J. Appl. Phys.* **122**, 135702 (2017).
- [29] J. Bizindavyi, A. S. Verhulst, Q. Smets, D. Verreck, B. Sorée, and G. Groeseneken, *IEEE J. Electron Devices Soc.* **6**, 633 (2018).
- [30] A. Schenk and S. Sant, *J. Appl. Phys.* **128**, 014502 (2020).
- [31] S.-Y. Chung, N. Jin, P. R. Berger, R. Yu, P. E. Thompson, R. Lake, S. L. Rommel, and S. K. Kurinec, *Appl. Phys. Lett.* **84**, 2688 (2004).
- [32] S.-L. Chen, P. B. Griffin, and J. D. Plummer, *IEEE Trans. Electron Devices* **56**, 634 (2009).
- [33] K.-J. Gan, C.-S. Tsai, and W.-L. Sun, *Electron. Lett.* **43**, 517 (2007).
- [34] R. Duane, A. Mathewson, and A. Concannon, *IEEE Electron Device Lett.* **24**, 661 (2003).
- [35] L. Fang, C. Qiu, H. Zhang, Y. Hu, and L.-M. Peng, *Adv. Electron. Mater.* p. 2101314 (2022).
- [36] K.-J. Gan, J.-J. Lu, W.-K. Yeh, Y.-H. Chen, and Y.-W. Chen, *Eng. Sci. Technol. an Int. J.* **19**, 888 (2016).
- [37] E. Şaşıoğlu and I. Mertig, *Negative differential resistance tunnel diode and manufacturing method* (2021), German Patent Application 102021206526.0.
- [38] E. Sasioglu and I. Mertig, *Bull. Am. Phys. Soc.* (2022).
- [39] J. Bardeen, *Phys. Rev. Lett.* **6**, 57 (1961).
- [40] R. Meservy and P. Tedrow, *Phys. Rep.* **238**, 173 (1994).
- [41] O. Gunnarsson, *Alkali-doped fullerenes: narrow-band solids with unusual properties* (World Scientific, 2004).
- [42] P. Hansmann, A. Toschi, G. Sangiovanni, T. Saha-Dasgupta, S. Lupi, M. Marsi, and K. Held, *Mott-hubbard transition in  $v_2o_3$  revisited* (2013).
- [43] N. Regnault, Y. Xu, M.-R. Li, D.-S. Ma, M. Jovanovic, A. Yazdani, S. S. P. Parkin, C. Felser, L. M. Schoop, N. P. Ong, et al., *Nature* **603**, 824 (2022).
- [44] S. Haastруп, M. Strange, M. Pandey, T. Deilmann, P. S. Schmidt, N. F. Hinsche, M. N. Gjerding, D. Torelli, P. M. Larsen, A. C. Riis-Jensen, et al., *2d Mater.* **5**, 042002 (2018).
- [45] M. N. Gjerding, A. Taghizadeh, A. Rasmussen, S. Ali, F. Bertoldo, T. Deilmann, N. R. Knøsgaard, M. Kruse, A. H. Larsen, S. Manti, et al., *2d Mater.* **8**, 044002 (2021).
- [46] N. Mounet, M. Gibertini, P. Schwaller, D. Campi, A. Merkys, A. Marrazzo, T. Sohier, I. E. Castelli, A. Cepellotti, G. Pizzi, et al., *Nat. Nanotechnol.* **13**, 246 (2018).
- [47] N. Janatipour, Z. Mahdaviifar, S. Noorizadeh, and G. Schreckenbach, *RSC Advances* **12**, 1758 (2022).
- [48] A. Ostovan, Z. Mahdaviifar, and M. Bamdad, *J. Mol. Liq.* **269**, 639 (2018).
- [49] A. Mishchenko, J. Tu, Y. Cao, R. V. Gorbachev, J. Wallbank, M. T. Greenaway, V. Morozov, S. Morozov, M. Zhu, S. Wong, et al., *Nat. Nanotechnol.* **9**, 808 (2014).
- [50] J. Shim, S. Oh, D.-H. Kang, S.-H. Jo, M. H. Ali, W.-Y. Choi, K. Heo, J. Jeon, S. Lee, M. Kim, et al., *Nat. Commun.* **7**, 1 (2016).
- [51] K.-H. Kim, H.-Y. Park, J. Shim, G. Shin, M. Andreev, J. Koo, G. Yoo, K. Jung, K. Heo, Y. Lee, et al., *Nanoscale Horiz.* **5**, 654 (2020).
- [52] Y.-C. Lin, R. K. Ghosh, R. Addou, N. Lu, S. M. Eichfeld, H. Zhu, M.-Y. Li, X. Peng, M. J. Kim, L.-J. Li, et al., *Nat. Commun.* **6**, 1 (2015).
- [53] T. Roy, M. Tosun, X. Cao, H. Fang, D.-H. Lien, P. Zhao, Y.-Z. Chen, Y.-L. Chueh, J. Guo, and A. Javey, *ACS Nano* **9**, 2071 (2015).
- [54] N. T. Duong, S. Bang, S. M. Lee, D. X. Dang, D. H. Kuem, J. Lee, M. S. Jeong, and S. C. Lim, *Nanoscale* **10**, 12322 (2018).
- [55] S. Smidstrup, T. Markussen, P. Vancaerfeld, J. Wellendorff, J. Schneider, T. Gunst, B. Verstichel, D. Stradi, P. A. Khomyakov, U. G. Vej-Hansen, et al., *J. Phys. Condens. Matter* **32**, 015901 (2020).
- [56] M. J. Van Setten, M. Giantomassi, E. Bousquet, M. J. Verstraete, D. R. Hamann, X. Gonze, and G.-M. Rignanese, *Comput. Phys. Commun.* **226**, 39 (2018).
- [57] J. P. Perdew, K. Burke, and M. Ernzerhof, *Phys. Rev. Lett.* **77**, 3865 (1996).
- [58] M. Büttiker, Y. Imry, R. Landauer, and S. Pinhas, *Phys. Rev. B* **31**, 6207 (1985).
- [59] C. Heil, M. Schlipf, and F. Giustino, *Phys. Rev. B* **98**, 075120 (2018).
- [60] S. Kim and Y.-W. Son, *Phys. Rev. B* **96**, 155439 (2017).
- [61] D. Huang, H. Nakamura, K. Küster, U. Wedig, N. B. M. Schröter, V. N. Strocov, U. Starke, and H. Takagi, *Phys. Rev. B* **105**, 245145 (2022), URL <https://link.aps.org/doi/10.1103/PhysRevB.105.245145>.
- [62] L. Cheng, C. Zhang, and Y. Liu, *Phys. Rev. Lett.* **125**, 177701 (2020).
- [63] A. Afzalian, *NPJ 2D Mater. Appl.* **5**, 1 (2021).
- [64] Y. Yin, C. Shao, H. Guo, J. Robertson, Z. Zhang, and Y. Guo, *IEEE Electron Device Lett.* **43**, 498 (2022).
- [65] See Supplemental Material at [arxiv.org](https://arxiv.org) for NbSe<sub>2</sub>/NbS<sub>2</sub> heterojunction and NbS<sub>2</sub> only device the electron difference density, *I-V* curves, the device density of states (DDOS) and electrostatic difference potential.
- [66] C. Qiu, F. Liu, L. Xu, B. Deng, M. Xiao, J. Si, L. Lin, Z. Zhang, J. Wang, H. Guo, et al., *Science* **361**, 387 (2018).
- [67] F. Liu, *Phys. Rev. Appl.* **13**, 064037 (2020).
- [68] E. G. Marin, D. Marian, M. Perucchini, G. Fiori, and G. Iannaccone, *ACS Nano* **14**, 1982 (2020).
- [69] D. Logoteta, J. Cao, M. Pala, P. Dollfus, Y. Lee, and G. Iannaccone, *Phys. rev. res.* **2**, 043286 (2020).
- [70] Z. Tang, C. Liu, X. Huang, S. Zeng, L. Liu, J. Li, Y.-G. Jiang, D. W. Zhang, and P. Zhou, *Nano Lett.* **21**, 1758 (2021).
- [71] W. Shin, G. Myeong, K. Sung, S. Kim, H. Lim, B. Kim, T. Jin, J. Park, K. Watanabe, T. Taniguchi, et al., *Appl. Phys. Lett.* **120**, 243506 (2022).

## Supplemental Material

Ersoy Şaşıoğlu<sup>1\*</sup> and Ingrid Mertig<sup>1,2</sup>

<sup>1</sup>*Institute of Physics, Martin Luther University  
Halle-Wittenberg, 06120 Halle (Saale), Germany*

<sup>2</sup>*Max Planck Institute of Microstructure Physics,  
Weinberg 2, 06120 Halle (Saale), Germany*

In Ref. <sup>1</sup> transport properties of the cold metal  $\text{MX}_2$  ( $\text{M}=\text{Nb, Ta}$ ;  $\text{X}=\text{Se, Te}$ ) heterojunctions have been studied by employing the DFT+NEGF method. The authors claim to get a promising PVCR value of 51 and extremely high peak current density ( $5.1 \times 10^4 \mu\text{A}/\mu\text{m}$ ) for an edge contact  $\text{NbSe}_2/\text{NbS}_2$  heterojunction device. To verify the findings of this paper we construct the same edge contact  $\text{NbSe}_2/\text{NbS}_2$  heterojunction (armchair orientation, see Figure S1a) and perform quantum transport calculations. Indeed we obtain a very similar  $I$ - $V$  curve (see Figure S2) with a peak current density of  $5 \times 10^4 \mu\text{A}/\mu\text{m}$ . However, the NDR effect obtained in this paper does not stem from a physical mechanism but from the numerical treatment of the current in the QuantumATK package, more specifically, from the division of the device in leads and scattering region, which artificially introduces electrostatic boundary conditions. The boundary conditions fix the bias voltage drop in an artificial manner, which can be seen in DDOS for the  $\text{NbSe}_2/\text{NbS}_2$  heterojunction device presented in Figure S3. As we discussed in main text for the case of lateral tunnel diode  $\text{AlI}_2/\text{MgI}_2/\text{AlI}_2$  the applied bias voltage  $V$  drops across the insulating tunnel barrier  $\text{MgI}_2$  (see Figure 6) and the potential is flat in the electrode regions, however the  $\text{NbSe}_2/\text{NbS}_2$  heterojunction does not have such a tunnel barrier and thus a small fraction of the applied voltage drops at the interface, where scattering takes place and the rest of the voltage artificially drops in a region close to the right electrode due to the electrostatic boundary conditions (see Figure S3). This artificial drop gives rise to an NDR effect, which is not physical but can be regarded as a numerical artifact. For a finite bias voltage  $V$  the NEGF calculations do not converge properly. Indeed, we get a proper convergence only for very small bias voltages less than  $0.1 \text{ V}$  and with increasing the bias voltage  $V$  even no proper convergence is reached above  $0.7 \text{ V}$  and thus cold metal-cold metal junctions do not provide any NDR effect without a tunnel barrier. Since both  $\text{NbSe}_2$  and  $\text{NbS}_2$  are metals with different work functions when they form a heterostructure an electrical double layer (electrical double layer in 3D) will be formed at the interface due to charge transfer (see Figure S1b). We would like to point out that the same effect occurs if we calculate the  $I$ - $V$  curve for a homogeneous system consisting of  $\text{NbS}_2$  only (see Figures S4 and S5).

---

\* Electronic address: ersoy.sasioglu@physik.uni-halle.de

<sup>1</sup> Y. Yin, C. Shao, H. Guo, J. Robertson, Z. Zhang, and Y. Guo, IEEE Electron Device Lett. **43**,

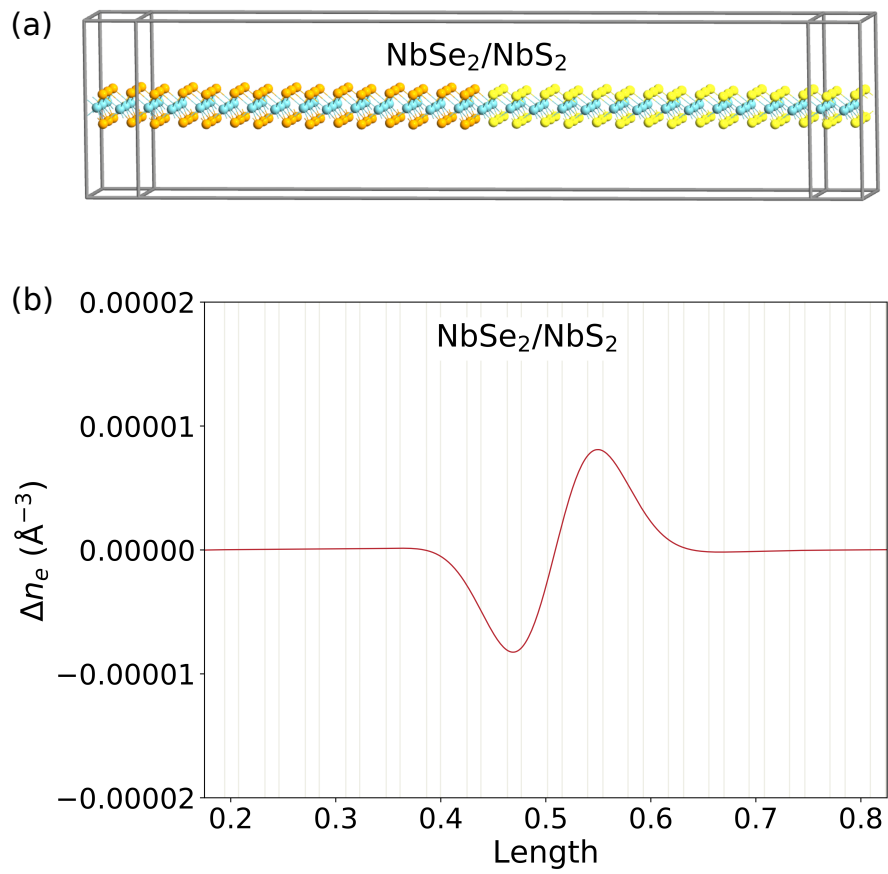


FIG. 1: (Color online) (a) The atomic structure of the lateral NbSe<sub>2</sub>/NbS<sub>2</sub> heterojunction (armchair orientation). (b) Electron difference density for the NbSe<sub>2</sub>/NbS<sub>2</sub> heterojunction.

498 (2022).

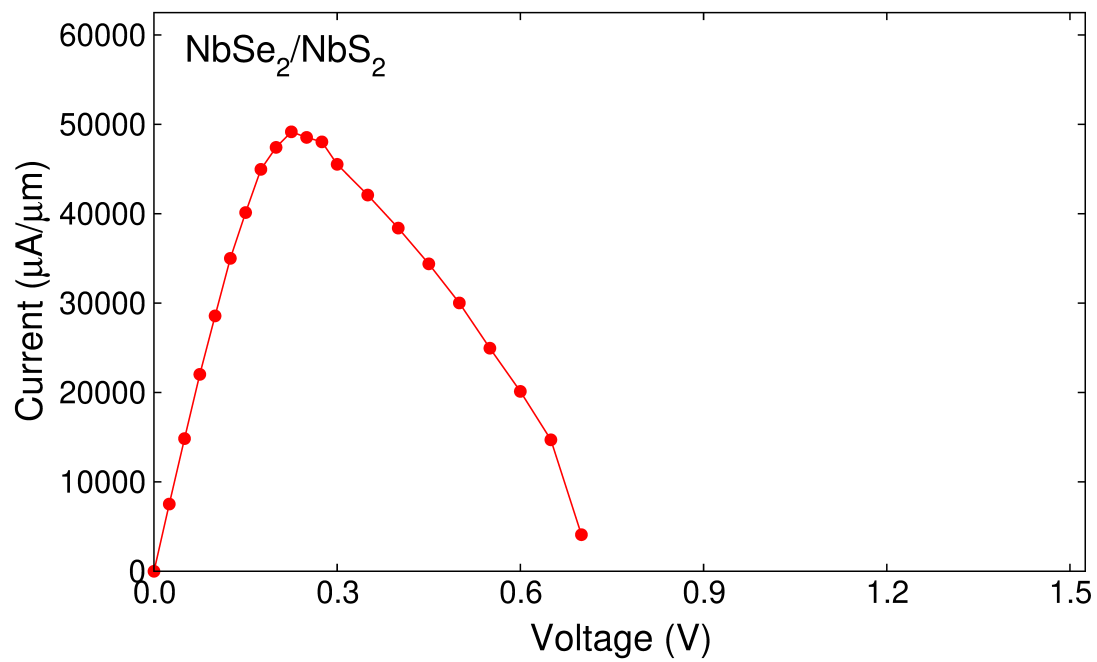


FIG. 2: (Color online). Calculated current-voltage ( $I$ - $V$ ) characteristics for the NbSe<sub>2</sub>/NbS<sub>2</sub> heterojunction in armchair orientation.

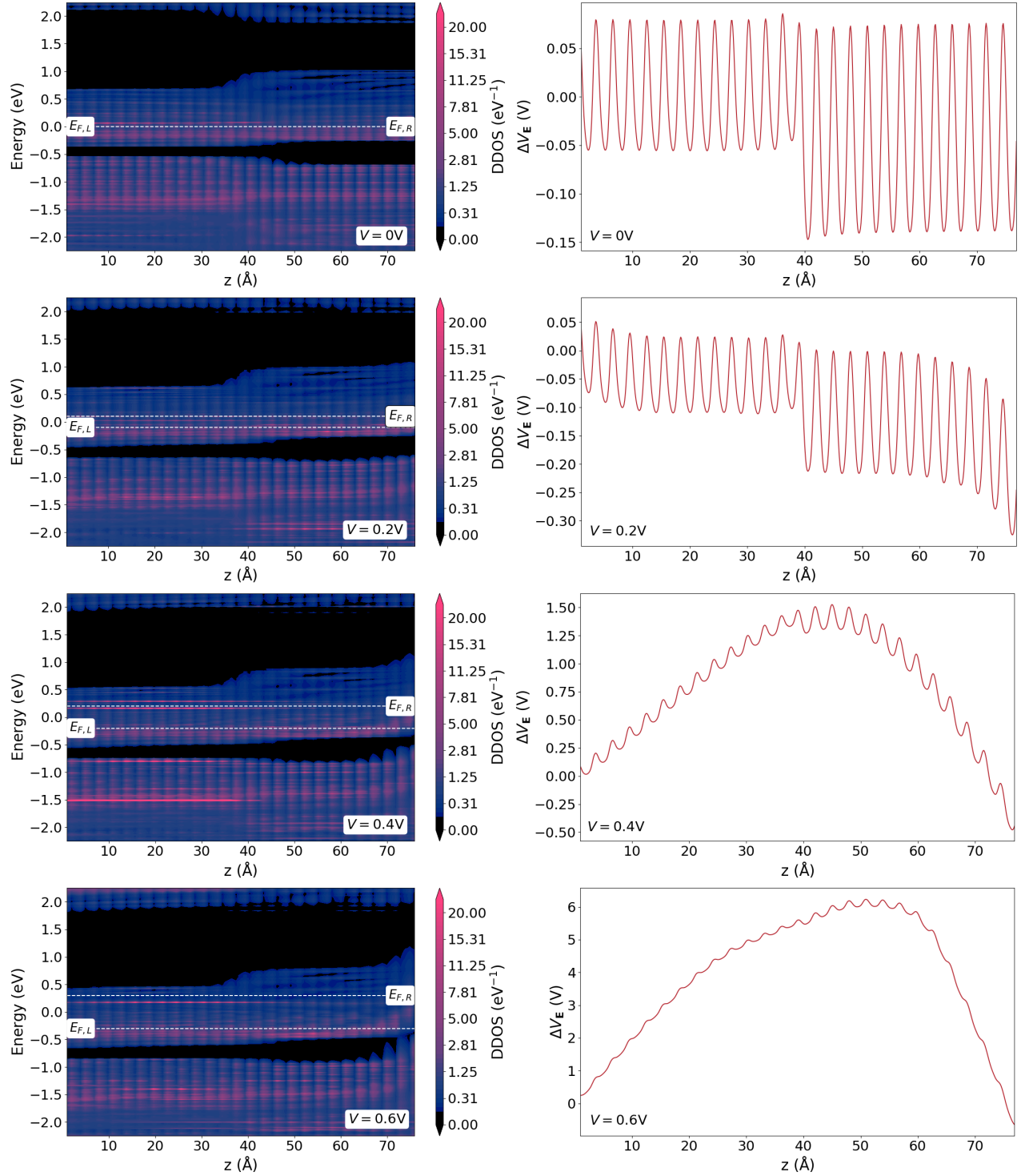


FIG. 3: (Color online) Left panels: Device density of states (DDOS) for the lateral NbSe<sub>2</sub>/NbS<sub>2</sub> heterojunction for different applied bias voltages calculated with the PBE method. The dashed lines display the Fermi level of the left and right electrodes. Right panels: Calculated electrostatic difference potential for different applied bias voltages.

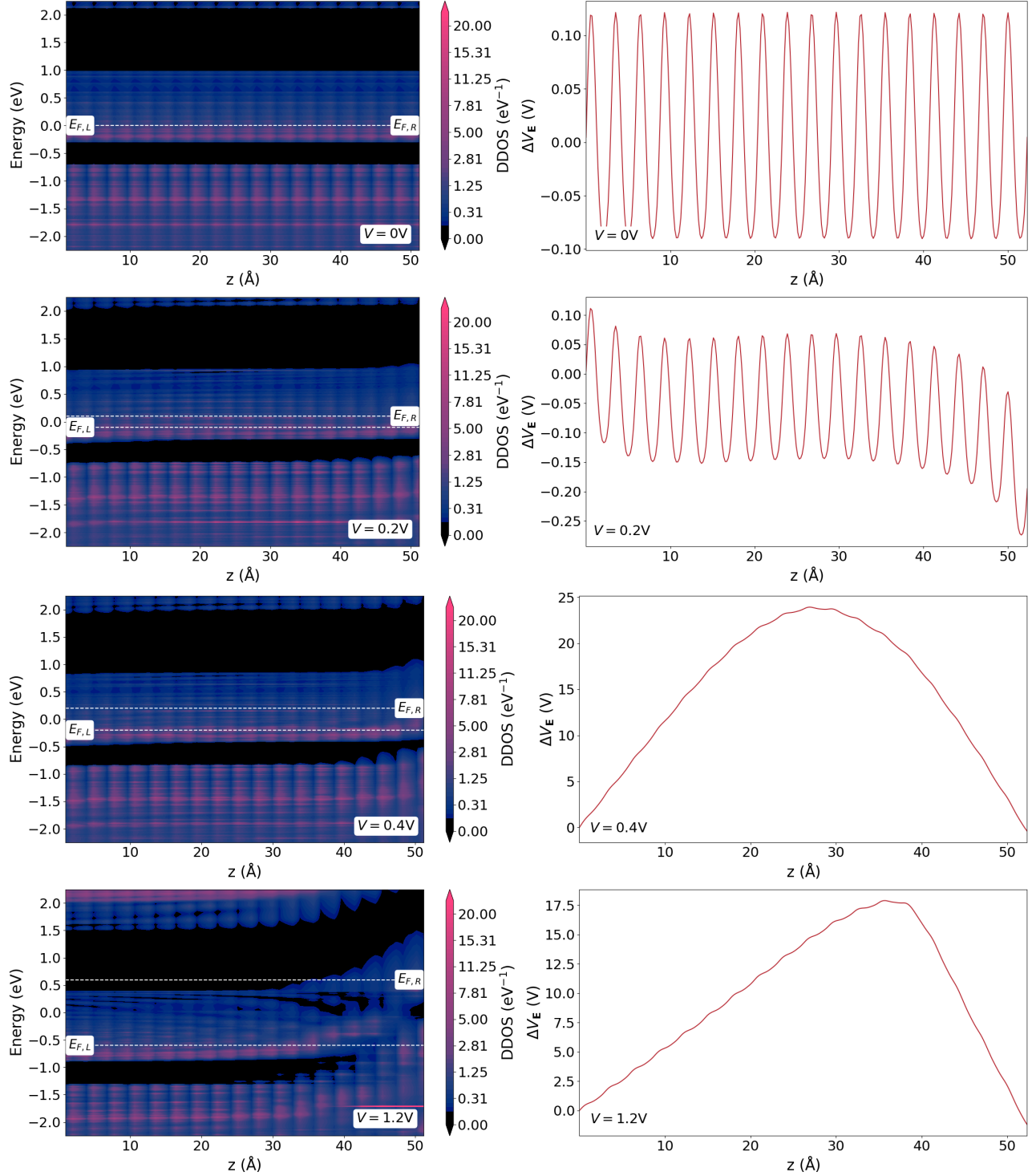


FIG. 4: (Color online). Left panels: Device density of states (DDOS) for the lateral homogeneous NbS<sub>2</sub> device for different applied bias voltages calculated with the PBE method. The dashed lines display the Fermi level of the left and right electrodes. Right panels: Calculated electrostatic difference potential for different applied bias voltages.

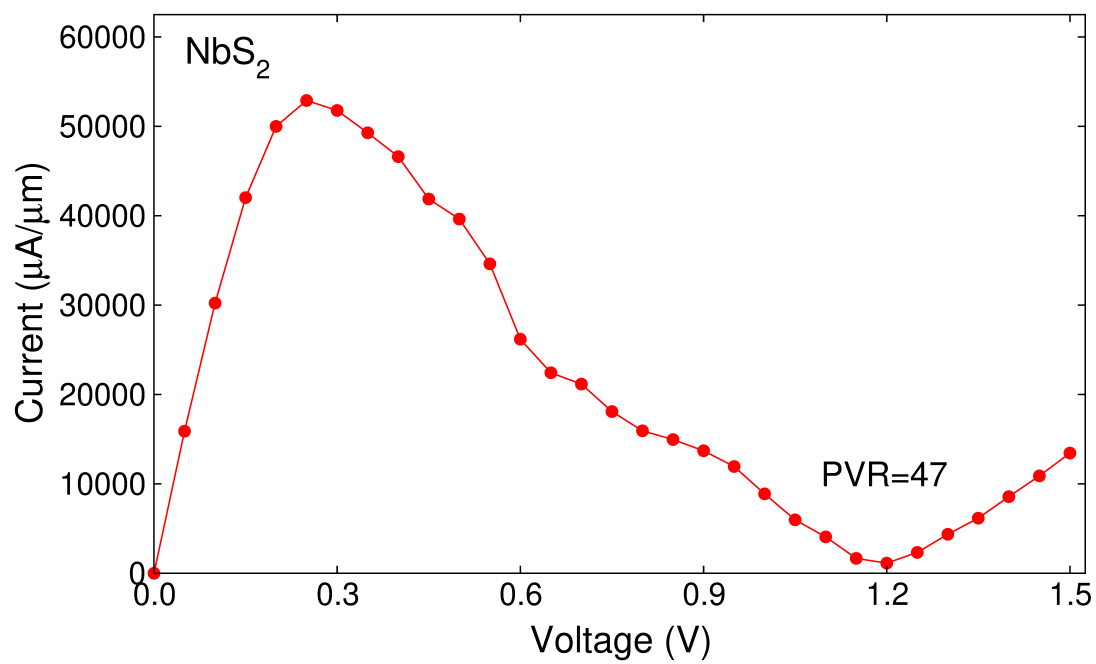


FIG. 5: (Color online). Calculated current-voltage ( $I$ - $V$ ) characteristics for the homogenous NbS<sub>2</sub> in armchair orientation.